Structural Characterization of Nanosized CeO$_2$−SiO$_2$, CeO$_2$−TiO$_2$, and CeO$_2$−ZrO$_2$ Catalysts by XRD, Raman, and HREM Techniques

Benjaram M. Reddy,* Ataullah Khan, and Pandian Lakshmanan

Inorganic and Physical Chemistry Division, Indian Institute of Chemical Technology, Hyderabad 500 007, India

Mimoun Aouine, Stéphane Loridant, and Jean-Claude Volta

Institut de Recherches sur la Catalyze−CNRS, 2 Avenue A. Einstein, 69626 Villeurbanne Cedex, France

Received: October 21, 2004

Structural characteristics of nanosized ceria−silica, ceria−titania, and ceria−zirconia mixed oxide catalysts have been investigated using X-ray diffraction (XRD), Raman spectroscopy, BET surface area, thermogravimetry, and high-resolution transmission electron microscopy (HREM). The effect of support oxides on the crystal modification of ceria cubic lattice was mainly focused. The investigated oxides were obtained by soft chemical routes with ultrahighly dilute solutions and were subjected to thermal treatments from 773 to 1073 K. The XRD results suggest that the CeO$_2$−SiO$_2$ sample primarily consists of nanocrystalline CeO$_2$ on the amorphous SiO$_2$ surface. Both crystalline CeO$_2$ and TiO$_2$ anatase phases were noted in the case of CeO$_2$−TiO$_2$ sample. Formation of cubic Ce$_{0.75}$Zr$_{0.25}$O$_2$ and Ce$_{0.6}$Zr$_{0.4}$O$_2$ (at 1073 K) were observed in the case of the CeO$_2$−ZrO$_2$ sample. Raman measurements disclose the fluorite structure of ceria and the presence of oxygen vacancies/Ce^{3+}. The HREM results reveal well-dispersed CeO$_2$ nanocrystals over the amorphous SiO$_2$ matrix in the cases of CeO$_2$−SiO$_2$, isolated CeO$_2$, and TiO$_2$ (anatase) nanocrystals, some overlapping regions in the case of CeO$_2$−TiO$_2$, and nanosized CeO$_2$ and Ce−Zr oxides in the case of CeO$_2$−ZrO$_2$ sample. The exact structural features of these crystals as determined by digital diffraction analysis of HREM experimental images reveal that the CeO$_2$ is mainly in cubic fluorite geometry. The oxygen storage capacity (OSC) as determined by thermogravimetry reveals that the OSC of the mixed oxide systems is more than that of pure CeO$_2$ and is system dependent.

Introduction

Cerium oxide containing materials have been the subject of numerous investigations in recent years because of their very broad range of applications in catalysis and in advanced ceramic materials.[1−9] The success of ceria in diverse applications is mainly due to its unique combination of an elevated oxygen transport capacity coupled with the ability to shift easily between reduced and oxidized states (Ce^{3+} ↔ Ce^{4+}).[8] Despite its widespread applications, the use of pure cerium dioxide is highly discouraged because it is poorly thermostable as it undergoes sintering at high temperatures, thereby losing its crucial oxygen storage and release characteristics.[8,10,11] To increase its temperature stability and ability to store and release oxygen during operations, other transition and non transition metal ions (Al^{3+}, Si^{4+}, Ti^{4+}, Zr^{4+}, etc.) are normally introduced into the ceria cubic structure.[12−21] The redox and catalytic properties of CeO$_2$ are strongly influenced when it is combined with other transition metals or rare earth oxides.

The redox and catalytic properties of ceria and its composite oxides are mainly dependent upon these main factors: particle size, phase modification, structural defects/distortion (lattice), and chemical nonstoichiometry. In general, reducing the particle size of a catalyst results in increasing surface area and changing its morphology, thus providing a larger number of more reactive edge sites. Especially when the particle size is decreased below 100 nm, the materials become nanophasic where the density of defects increases so that up to half (50%) of the atoms are situated in the cores of defects (grain boundaries, interphase boundaries, dislocations, etc.). The high density of defects in nanophase materials provides a large number of active sites for gas−solid catalysis, while the diffusivity through the nanometer-sized interfacial boundaries promotes fast kinetics of the catalyst activation and reactions.[1,22−29] Thus, there are several advantages for switching from conventional to nanosized materials.

Motivated by the unique and favorable characteristics of ceria-based mixed oxides and solid solutions for various applications, an effort has been made in the present study to understand the nanostructural evolution of CeO$_2$−SiO$_2$, CeO$_2$−TiO$_2$, and CeO$_2$−ZrO$_2$ oxides. Although the CeO$_2$−Al$_2$O$_3$ combination has been extensively investigated in the literature for the purpose of automotive pollution control,[30−37] supports other than alumina have not been thoroughly investigated even though they have many potential applications other than three-way catalysts.[14,15,32,38,39] Since silica, titania, and zirconia are the most widely employed supports as well as catalysts for several applications, we undertook the present investigation to stabilize ceria over the surface of these oxides and subjected them to thermal treatments. These effects were systematically investigated using X-ray diffraction (XRD), Raman spectroscopy, high-resolution transmission electron microscopy (HREM), and other techniques. The oxygen storage capacity of the mixed oxides was determined by thermogravimetry and correlated with the characterization results.

---

* Corresponding author. E-mail: bmreddy@iict.res.in.

3356 *J. Phys. Chem. B, Vol. 109, No. 8, 2005*

Reddy et al.

Experimental Section

Preparation of Samples. Soft chemical routes with ultra-highly dilute solutions were employed to prepare the investigated CeO_2-SiO_2, CeO_2-TiO_2, and CeO_2-ZrO_2 mixed oxides (1:1 mole ratio based on oxides). To make CeO_2-TiO_2, the requisite quantities of $CeCl_3 \cdot 7H_2O$ (99.0%, Aldrich) and $TiCl_4$ (99.9%, Aldrich) were dissolved separately in excess double-distilled water and mixed together. To obtain CeO_2-ZrO_2, the desired quantities of ammonium cerium(IV) nitrate (Loba Chemie, GR grade) and zirconium(IV) nitrate (Fluka, AR grade) were dissolved separately and mixed together. To prepare CeO_2-SiO_2, the requisite quantities of cerium ammonium nitrate (Loba Chemie, GR grade), dissolved separately in deionized water, and colloidal silica (40 wt %, Fluka, AR grade) were mixed together. Dilute aqueous ammonia was added gradually drop-wise to the aforementioned mixture solutions, with vigorous stirring, until precipitation was complete (pH 8). The obtained precipitates were filtered off and washed several times with double-distilled water until free from anion impurities. The obtained cakes were oven dried at 393 K for 12 h and finally calcined at 773 K for 5 h. Some portions of the calcined mixed oxides were once again heated at 873, 973, and 1073 K for 5 h. The rate of heating as well as cooling was always maintained at 5 K min^{-1}.

Characterization of Samples. Powder X-ray diffraction (XRD) patterns were recorded on a Siemens D-500 diffractometer using a nickel-filtered Cu Kα (0.15418 nm) radiation source. The intensity data were collected over a 2θ range of $3-80°$ with a 0.02° step size and using a counting time of 1 s per point. Crystalline phases were identified by comparison with the reference data from ICDD files. The average crystallite size of CeO_2 was estimated with the help of the Debye−Scherrer equation using the XRD data of all prominent lines.[40]

The Raman spectra were recorded on a DILOR XY spectrometer equipped with a CCD detector at ambient temperature. The emission line at 514.5 nm from an Ar$^+$ ion laser (Spectra Physics) was focused, with an analyzing spot about 1 μm, on the sample under the microscope. The power of the incident beam on the sample was 3 mW. The time of acquisition was varied according to the intensity of the Raman scattering. The wavenumbers obtained from spectra are accurate to within 2 cm^{-1}.

High-resolution electron microscopy was carried out with a JEM 2010 (Cs = 0.5 mm) microscope. The accelerating voltage was 200 kV with LaB$_6$ emission current, a point resolution of 0.195 nm, and a useful limit of EDS LINK-ISIS. Energy-dispersive X-ray microanalysis (EDX) was conducted using a probe size of 25 nm to analyze grains of the phases; simultaneous analysis of grains of two phases was avoided. Samples were sonically dispersed in ethanol and deposited on a holey carbon copper grid before examination.

The potential oxygen storage capacity (OSC) was tested by oxygen release characteristics of the powders in the temperature range 573−1073 K. The change in the weight of the sample was monitored by thermogravimetry (TG) under cyclic heat treatments in flowing nitrogen or dry air. A commercial Netzsch (Luxx, STA, 409 PC, Germany) TG-DTA analyzer was employed for this purpose. The heat cycle consisted of heating the sample to 1073 K, cooling to 423 K, and again heating to 1073 K. All heating and cooling rates were 5 K min^{-1}. The weight loss of sample during the second heating cycle was used to measure the oxygen release properties (δ). This technique of OSC evaluation is essentially similar to that described previously.[41,42]

TABLE 1: BET Surface Area and Crystallite Size Measurements of CeO_2-SiO_2, CeO_2-TiO_2, and CeO_2-ZrO_2 Samples Calcined at 773 and 1073 K

calcination temp (K)	surf. area (m^2 g^{-1})	cryst size^a (nm)
	CeO_2-SiO_2	
773	147	3.2^b
1073	54	6.0^b
	CeO_2-TiO_2	
773	59	10.0^b
1073	31	14.1^b
	CeO_2-ZrO_2	
773	84	4.7^c
1073	36	5.5^c

^{a} From Scherrer equation. ^{b} CeO_2. ^{c} $Ce_{0.75}Zr_{0.25}O_2$.

The BET surface areas were determined by N$_2$ physisorption using a Micromeritics Gemini 2360 Instrument. Prior to analysis, the samples were oven dried at 393 K for 12 h and flushed with argon gas for 2 h.

Results and Discussion

The N$_2$ BET surface areas of CeO_2-SiO_2, CeO_2-TiO_2, and CeO_2-ZrO_2 samples calcined at 773 and 1073 K are presented in Table 1. The 773 K calcined samples exhibit reasonably high specific surface area. However, with increasing calcination temperature there is a continuous decrease and the decrease is greater after calcination at 1073 K. The decrease varies between 48 and 63% depending on the sample under consideration. The observed decrease in the surface area with increasing calcination temperature could be due to various reasons such as better crystallization of ceria, formation of various mixed oxide phases, and sintering. In particular, the CeO_2-SiO_2 combination shows a high specific surface area among other samples, as it is well-known that silica is an effective surface area stabilizer. The efficiency of foreign cations (Si^{4+}, Ti^{4+}, and Zr^{4+}) in preventing the loss of specific surface area at high temperatures could be related to variations in the rate of crystal growth. The nature and concentration of the foreign cations present in the system govern this variation.[20]

Various prepared samples calcined from 773 to 1073 K were subjected to X-ray powder diffraction analysis. The XRD profiles of the samples calcined at 773 and 1073 K are shown in Figure 1. As can be noted from this figure, the ceria−silica mixed oxide (Figure 1a) calcined at 773 K exhibits poor crystallinity. Only the broad diffraction lines due to CeO_2 (PDF-ICDD 34-0394) can be seen. With increasing calcination temperature a gradual increase in the intensity of the lines due to better crystallization of cerium oxide is observed. No extra lines due to SiO_2 or mixed phases between ceria and silica are found. Rocchini et al.[20,38,39] recently reported the formation of an intermediate $Ce_{9.33}(SiO_4)_6O_2$ phase (investigated by XRD, TEM, and other techniques) between ceria and silica that on suitable treatment decomposes into amorphous silica and smaller crystallites of ceria. This intermediate phase was attributed to the enhanced textural and thermal stability of these mixed oxides. To confirm its formation, a reference sample was prepared from a stoichiometric combination of CeO_2 (82%) and SiO_2 (18%) oxides to give $Ce_{9.33}(SiO_4)_6O_2$.[38] The absence of this compound in the present study could be due to a different preparation method adopted and the lower calcination temperatures employed. The XRD profiles of CeO_2-TiO_2 sample calcined at 773 and 1073 K (Figure 1b) provide typical diffraction patterns of cubic CeO_2 along with few less intense peaks due to TiO_2 anatase phase (PDF-ICDD 21-1272). With
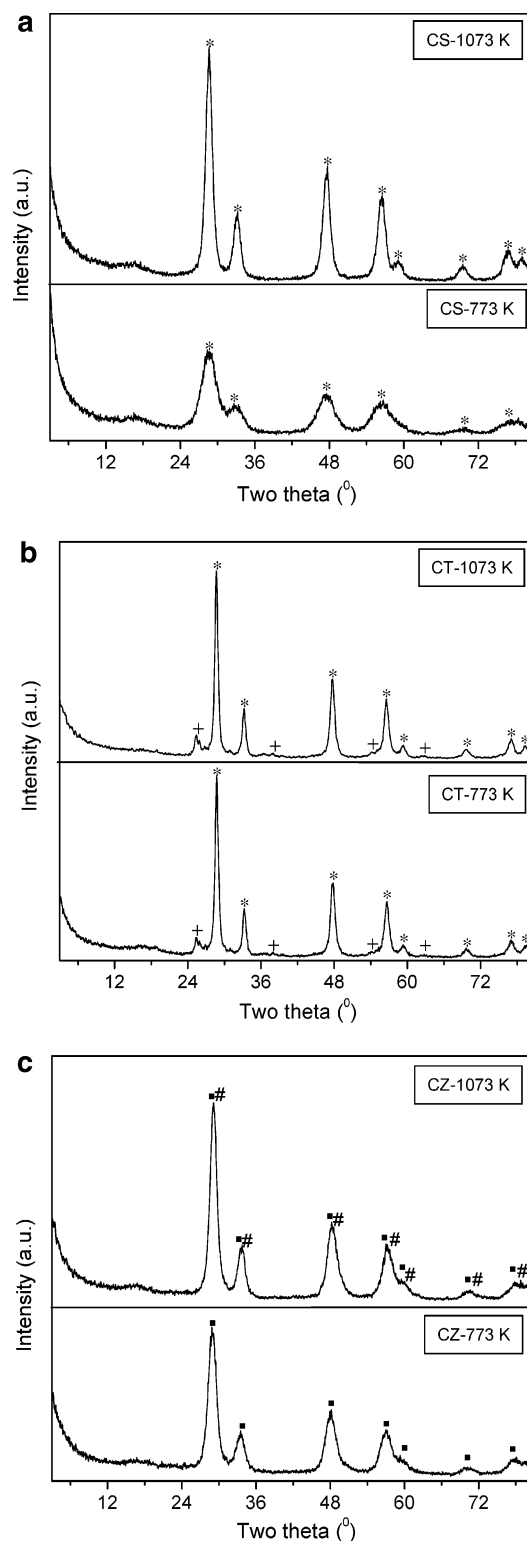
Figure 1. Powder X-ray diffraction (XRD) patterns of CeO$_2$−SiO$_2$ (CS), CeO$_2$−TiO$_2$ (CT), and CeO$_2$−ZrO$_2$ (CZ) mixed oxides calcined at 773 and 1073 K. Peaks legend: *, lines due to CeO$_2$; ■, lines due to Ce$_{0.75}$Zr$_{0.25}$O$_2$; #, lines due to Ce$_{0.6}$Zr$_{0.4}$O$_2$; + lines due to TiO$_2$ anatase.

increasing calcination temperature a slight increase in the intensity of the lines due to both these phases is observed. On heating an appropriate mixtures of solids containing Ce and Ti at 1523 K, manifestation of various Ce−Ti−O oxides, namely, Ce$_2$TiO$_5$, Ce$_2$Ti$_2$O$_7$, and Ce$_4$Ti$_9$O$_{24}$, were recently reported by Preuss and Gruehn.[43] It is a known fact in the literature that transformation of anatase to rutile is thermodynamically feasible beyond 873 K in impurity-free TiO$_2$ samples.[44] However, there

is no evidence regarding the formation of rutile phase even at 1073 K in the present study. The absence of Ce−Ti−O crystalline compounds and TiO$_2$ rutile phase could again be due to a different preparation method adopted and the lower calcination temperatures employed in the present investigation.[45] It is also a well-established fact in the literature that incorporation of additives such as V$_2$O$_5$ and MoO$_3$[16,46] accelerate anatase to rutile phase transformation whereas SiO$_2$[47] and Ga$_2$O$_3$[48] retard the same. The present results suggest that CeO$_2$ also inhibits the anatase to rutile phase modification. The XRD profiles of CeO$_2$−ZrO$_2$ sample calcined at 773 K (Figure 1c) also reveal relatively poor crystallinity. Only the broad diffraction lines due to a cubic fluorite type phase with the composition Ce$_{0.75}$Zr$_{0.25}$O$_2$ (PDF-ICDD 28-0271) are identified. With increasing calcination temperature from 773 to 1073 K, an increase in the intensity of the lines due to better crystallization of this phase is noted. A slight shift in the peak positions ($2\theta = 28.90-29.32°$) could be noted, which indicates that along with particle growth some compositional changes are also taking place. The observed additional broad diffraction patterns at 1073 K could be assigned to Ce$_{0.6}$Zr$_{0.4}$O$_2$ phase (PDF-ICDD 38-1439). This is primarily due to a progressive increase of zirconia content into the ceria unit cell, since the ionic radius of zirconium (0.84 Å) is smaller than that of cerium cation (0.97 Å).[8,21] Incorporation of zirconium ion into the ceria lattice leads to shrinkage of the lattice.[13,21] Within the detection limits of XRD technique, there is no evidence for the presence of t-ZrO$_2$ or m-ZrO$_2$ phases.

Crystallite sizes (D_{XRD}) of CeO$_2$ in CeO$_2$−SiO$_2$ and CeO$_2$−TiO$_2$ samples and of Ce$_{0.75}$Zr$_{0.25}$O$_2$ in CeO$_2$−ZrO$_2$ as a function of calcination temperature are summarized in Table 1. The CeO$_2$ crystallization apparently depends on both the calcination temperature and the type of mixed oxide system. The phenomenon of crystallite growth can be explained variously in each individual system. The precipitation of ceria along with colloidal silica could yield smaller crystallites of ceria on the surface of silica, which coalesce under the impact of calcination thus accounting for an increase in the crystallite size. In the case of the Ce−Ti system, the cubic ceria structure prevailed along with the TiO$_2$ (anatase) modification. In particular, the Ce−Ti combination exhibited well-crystallized patterns with bigger crystallites probably due to mutual influence. The formation of solid solutions between CeO$_2$ and ZrO$_2$ retards the crystallite growth, thus paving the way for the formation of thermodynamically more stable phases.

The Raman spectra of various samples calcined at 773 and 1073 K are shown in Figure 2. The CeO$_2$ normally exhibits a strong band at 462 cm^{-1} due to the F$_{2g}$ Raman active mode of fluorite structure.[36] Besides, it also exhibits a weak band around 260 cm^{-1} and a shoulder at ∼600 cm^{-1}, which are attributed respectively to the normal Raman inactive (IR active) transverse and longitudinal optical phonon modes at the Brillouin zone center.[49] As presented in Figure 2a, the Raman spectrum of CeO$_2$−SiO$_2$ sample calcined at 773 K shows a prominent peak at ∼457 cm^{-1} and a weak band at ∼600 cm^{-1}. The band at ∼457 cm^{-1} corresponds to the triply degenerate F$_{2g}$ mode and can be viewed as a symmetric breathing mode of the oxygen atoms around cerium ions.[50] With increasing calcination temperature from 773 to 1073 K, the band at 457 cm^{-1} has been shifted to ∼461 cm^{-1}, sharpened, and become more symmetrical. This could be due to better crystallization of ceria at higher calcination temperatures as observed from XRD measurements. The weak band near 600 cm^{-1} should not be observed by Raman spectroscopy, but the presence of some defects can involve relaxation of selection rules and then the
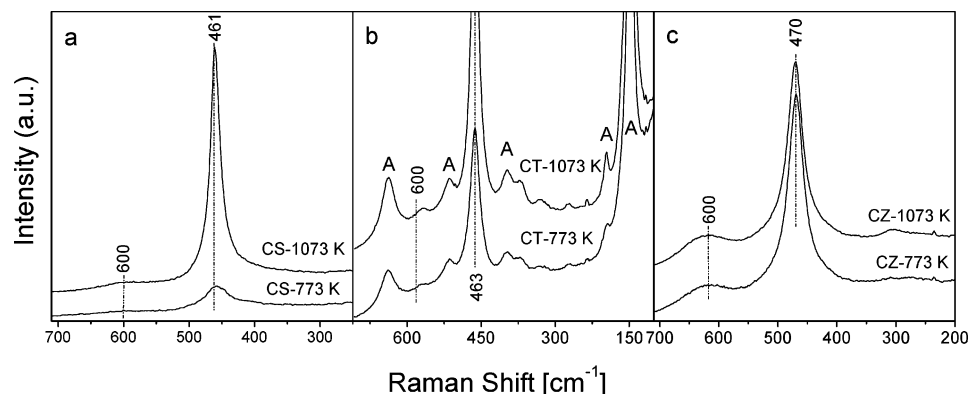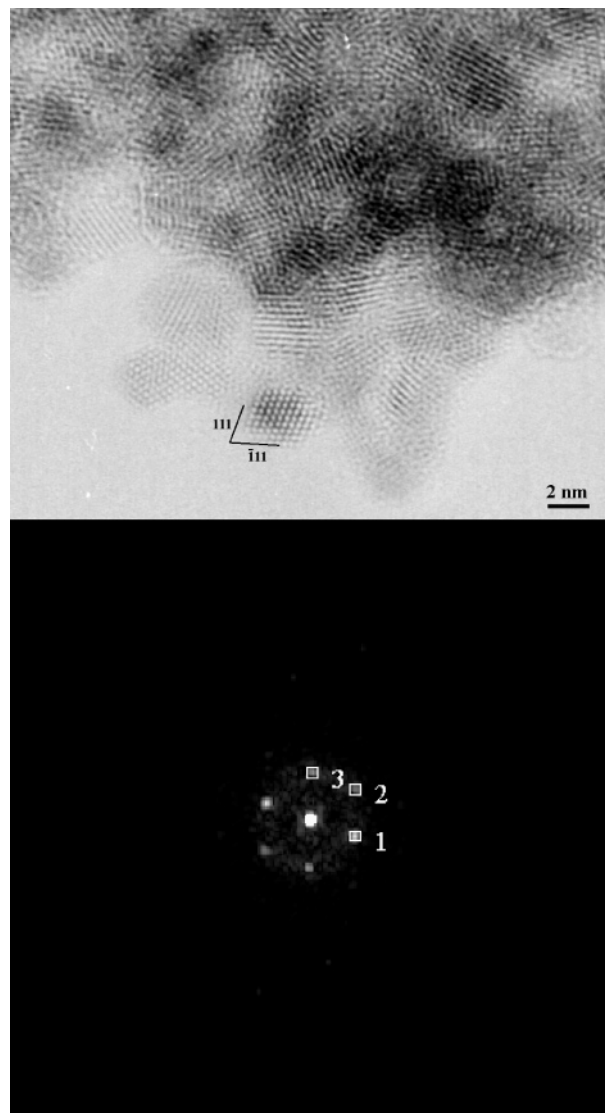
Figure 2. Raman spectra of CeO_2-SiO_2, CeO_2-TiO_2, and CeO_2-ZrO_2 mixed oxides calcined at 773 and 1073 K. Bands corresponding to TiO_2 anatase are indicated (A).
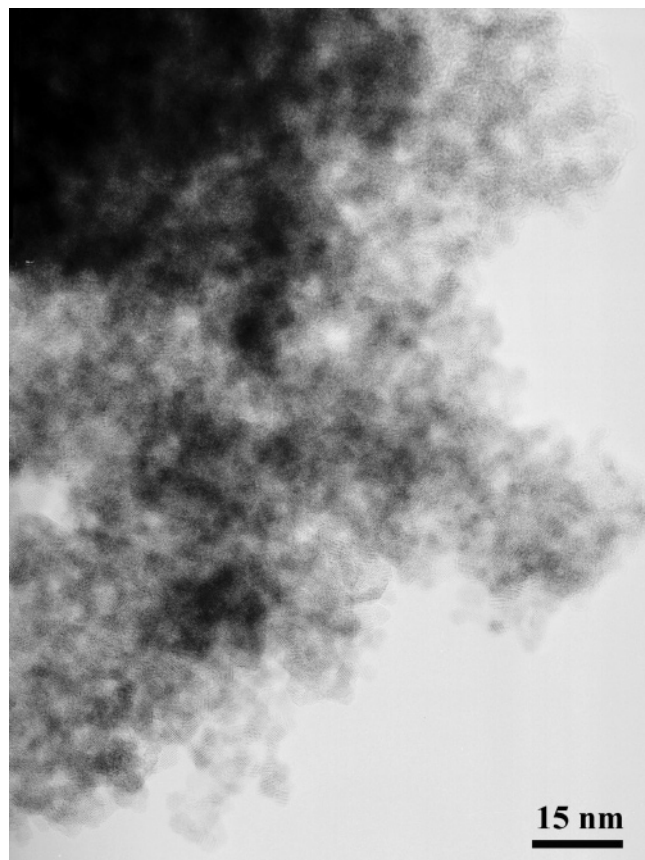
Figure 3. TEM image of CeO_2-SiO_2 sample calcined at 773 K.

Figure 4. HREM image of CeO_2-SiO_2 sample calcined at 773 K. The digital diffraction pattern (DDP) obtained from the corresponding image is also shown.

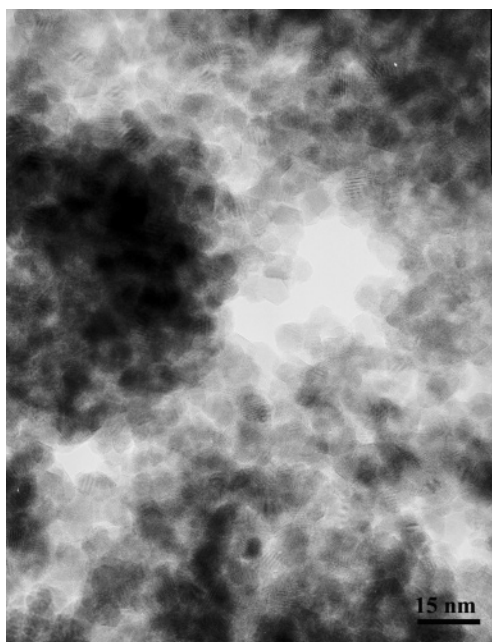observation of such bands. In particular, this band was observed in nanosized samples and was linked to oxygen vacancies in the CeO_2 lattice.[50,51] The increase in the intensity of this band with increasing calcination temperature could be to due to an increase in the concentration of oxygen vacancy defects.

The Raman spectrum of CeO_2-TiO_2 sample calcined at 773 K (Figure 2b) shows typical spectra of TiO_2 anatase (space group $I4_1/amd$)[44] and CeO_2.[50] The Raman bands pertaining to anatase phase appear at 147, 196, 397, 514, and 638 cm^{-1}, while ceria exhibits peaks at 272, 463, and ~570 cm^{-1}, which are in agreement with literature reports.[50] McBride et al. reported the Raman spectra of $Ce_{1-x}RE_xO_{2-y}$ (RE = rare earth) solid solutions and found that the F_{2g} mode becomes asymmetric with the presence of a long low-frequency tail as x increases; there is also a weak shoulder on the high-frequency side of the band, which would evolve into a broad peak at ca. 570 cm^{-1} for a larger x.[51] As mentioned earlier, this broad peak is associated

with oxygen vacancies in the solid solutions.[52,53] In agreement with XRD measurements, there is no evidence about the TiO_2 rutile phase and the formation of detectable compounds between ceria and titania. The spectra of CeO_2-ZrO_2 samples calcined at 773 and 1073 K are again dominated by a strong band at ~470 cm^{-1} due to the F_{2g} vibration of the fluorite type lattice and a less prominent broad band at ~600 cm^{-1} (Figure 1c). It

Nanosized CeO$_2$−SiO$_2$, −TiO$_2$, and −ZrO$_2$ Catalysts

J. Phys. Chem. B, Vol. 109, No. 8, 2005 **3359**

Figure 5. TEM image of CeO$_2$−SiO$_2$ sample calcined at 1073 K.

is apparent from Raman results that ceria−zirconia support is mostly in the cubic form and does not show signs of tetragonal modification. The shift in the Raman frequency to higher wavenumbers could be due to incorporation of zirconia into the ceria lattice as evidenced by XRD results.

To explore the structural features at the atomic level, HREM studies were performed on some selected representative samples. The TEM global view of the CeO$_2$−SiO$_2$ sample calcined at 773 K is shown in Figure 3. A closer inspection of the image reveals the existence of smaller crystals (∼3−4 nm) dispersed over an amorphous matrix with different contrasts. For deeper insight, the analyses of high-resolution images were undertaken to establish the structure of the particles. Figure 4 shows the HREM image of the sample subjected to the same thermal treatment. The contrast observed in the experimental image is associated with the face centered cubic structure (fluorite) of the cerium oxide. Well-crystallized CeO$_2$ grains mixed with SiO$_2$ (amorphous matrix) are mainly observed.[38,54,55] The presence of bidimensional dark spots can be clearly noted. The digital diffraction pattern (DDP) obtained from the experimental image is also shown in Figure 4. The different spots that are present account for the existence of periodic contrasts in the original experimental micrographs, which correspond to different sets of atomic planes of the crystalline structure. The geometric arrangement of these reflections are directly related to the structural aspects of the analyzed crystals. Because of this the DDPs are very useful for phase recognition.[56,57] The spots labeled 1, 2, and 3 in the DDP correspond to the interplanar spacings of 3.2, 2.7, and 3.1 Å, respectively, which correspond to the (111), (200), and (1-1-1) planes of ceria in cubic fluorite structure. Energy-dispersive X-ray microanalysis (EDX) was performed to gain information on the composition of the surface, which revealed the presence of Ce and Si in stoichiometric proportions. Taking into account the analysis performed on the experimental images, it can be inferred that a good dispersion of the CeO$_2$ nanophases on the surface of partly amorphous silica matrix has been obtained. This dispersed phase is present in the form of small crystals of 3−4 nm average sizes.

Figure 5 shows a representative TEM image of the CeO$_2$−SiO$_2$ sample calcined at 1073 K. The presence of ceria nanocrystals dispersed over the large silica grains is mainly seen
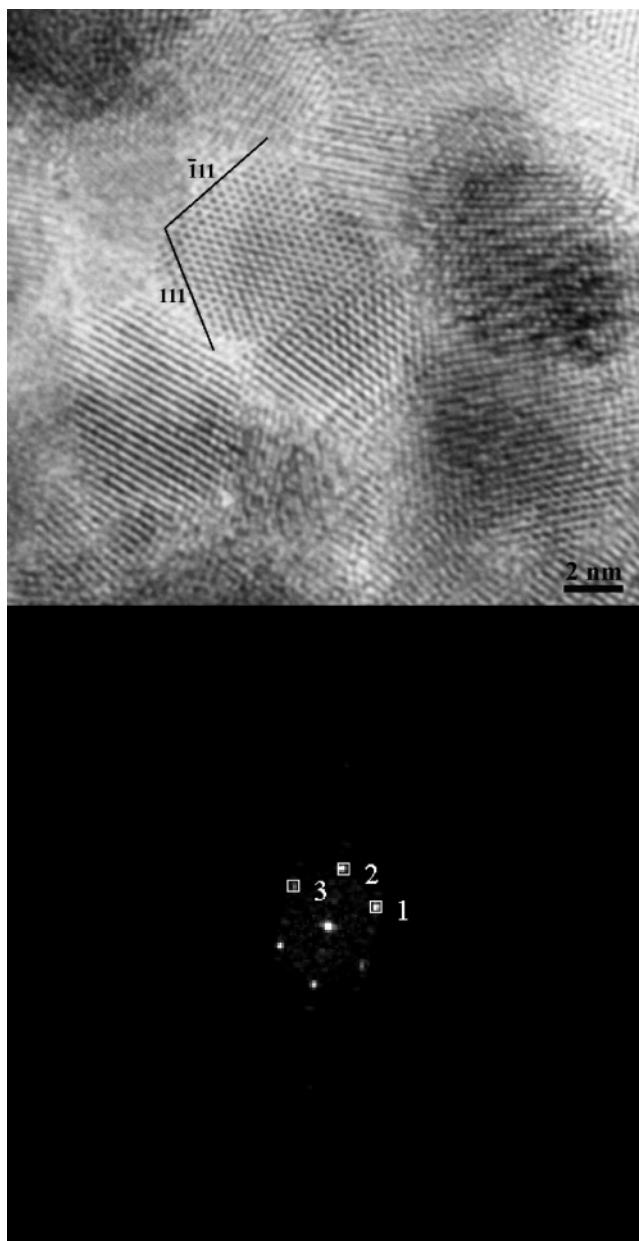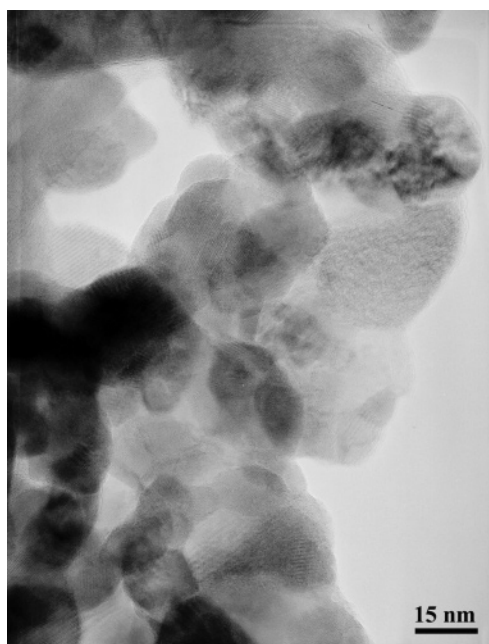

Figure 6. HREM image of CeO$_2$−SiO$_2$ sample calcined at 1073 K. The corresponding digital diffraction pattern (DDP) is also shown.

from this image. The dispersed ceria phase seems to be slightly different when compared to that of the sample calcined at 773 K. Also, the crystallinity of the sample has increased (in line with XRD). In this case, as revealed by the analysis of the subsequent images, the mean size of the CeO$_2$ crystals increased from 3−4 nm to a value close to 6−10 nm. The HREM image and the corresponding digital diffraction pattern are depicted in Figure 6. The fringes appearing in the micrograph allow for the identification of the crystallographic spacing of the CeO$_2$ nanocrystallites. In the HREM image, the ceria crystallites can be discriminated as patches of parallel lattice fringes with a distance of ∼3.2 Å [CeO$_2$ (111) lattice planes]. In this image also the bidimensional distribution can be clearly observed. The digital diffraction pattern consists of three diffraction spots labeled 1, 2, and 3 around the undeflected central spot. These represent (111), (200), and (1-1-1) planes of cubic fluorite ceria with 3.1, 2.7, and 3.1 Å interplanar spacings, respectively. The EDX analyses to a greater extent corroborate the stoichiometry of the sample. However, in certain areas the dispersed ceria
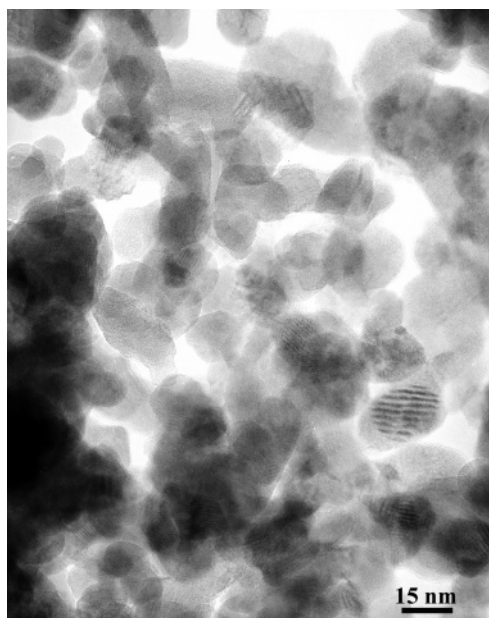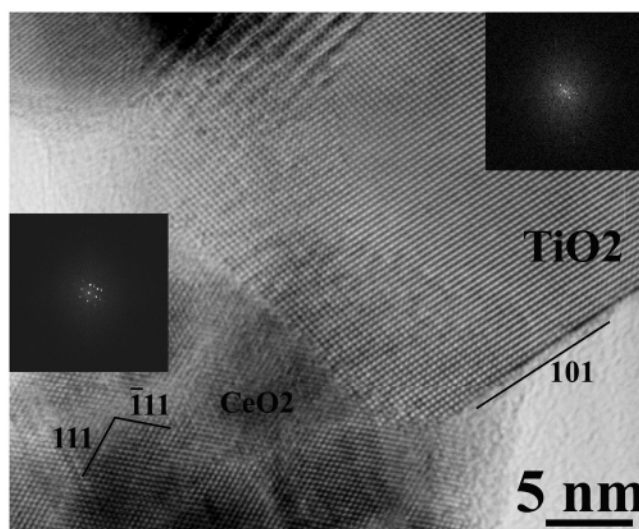
Figure 7. TEM image of CeO_2–TiO_2 sample calcined at 773 K.

Figure 8. TEM image of CeO_2–TiO_2 sample calcined at 1073 K.

phase was completely absent, which indicates the influence of high temperature treatment on the surface segregation of ceria nanoparticles.

The electron micrographs of the CeO_2–TiO_2 sample calcined at 773 and 1073 K are shown in Figures 7 and 8, respectively. The low temperature calcined sample revealed well-crystallized grains of CeO_2 and TiO_2 with approximate grain size of ~20 nm. With an increase in calcination temperature the size of ceria grains increased from 20 to ~50 nm while that of titania increased to ~35 nm. The fringes observed in the micrographs can be attributed to the (111) and (101) crystallographic planes of CeO_2 and TiO_2 anatase phases, respectively. The HREM image of the sample calcined at 1073 K, shown in Figure 9, clearly reveals three distinct regions: in the lower left, the ceria-only region; in the upper right, the titania-only region; in between, the intermediate region formed by overlapping of both ceria and titania grains. The corresponding DDPs are also shown as insets in Figure 9. Analyses of the spots labeled 1, 2, 3, and
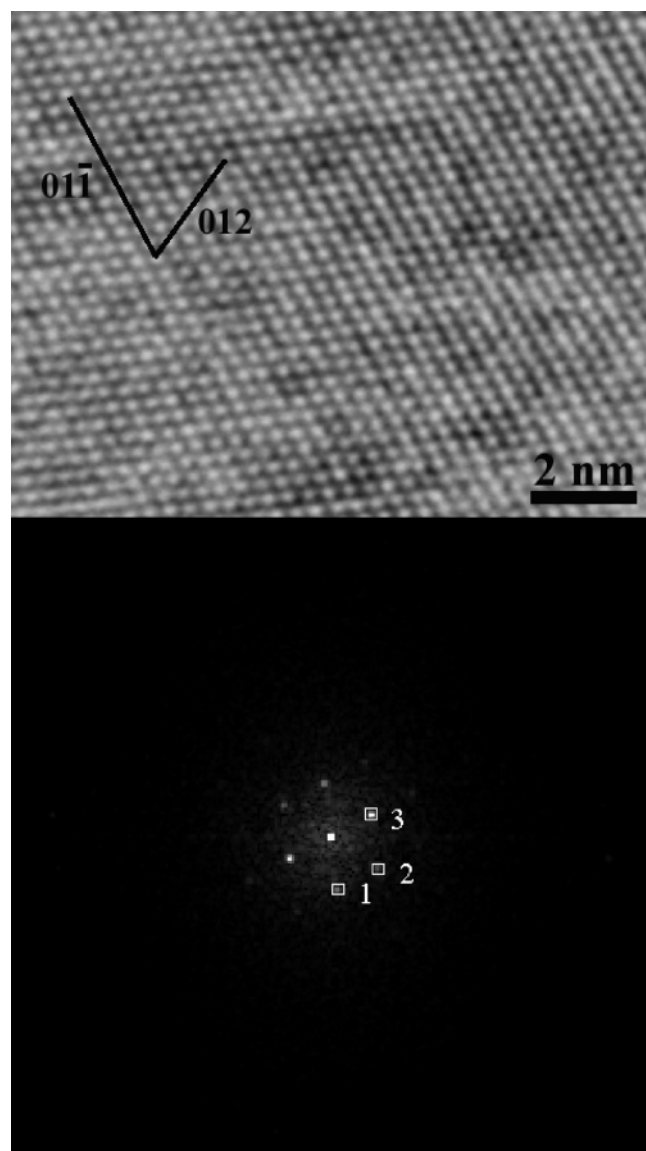

Figure 9. HREM image of CeO_2–TiO_2 sample calcined at 1073 K. The insets in the image are digital diffraction patterns (DDPs) obtained from the corresponding particles.

4 (top right inset) reveal the typical diffraction pattern of the anatase TiO_2, with interplanar spacings of 3.42, 2.66, 3.54, and 2.3 Å corresponding to (101), (110), (01-1), and (-11-2) planes, respectively.[58] The other DDP (bottom left inset) reveals the typical diffraction pattern of CeO_2 phase. The respective interplanar spacings and the corresponding planes for the spots labeled 1, 2, and 3 are as follows: 3.0 Å (111), 2.6 Å (200), and 3.1 Å (1-1-1).

A further well-resolved HREM image along with its DDP corresponding to the titania region is shown in Figure 10. A clear bidimensional distribution could be seen from this image. The spots labeled 1, 2, and 3 correspond to (003), (012), and (01-1) planes of titania anatase with interplanar spacings of 3.0, 2.9, and 3.5 Å, respectively, taken along the [100] zone axis. The presence of dark and light intermittent bands observed in the micrographs (Figures 7 and 8) could be due to a diffraction phenomenon caused by the superimposition of CeO_2 and TiO_2 grains.[59] The EDX analyses revealed the presence of Ce and Ti in appropriate stoichiometries. In particular, the EDX of 1073 K calcined sample confirmed the presence of ceria-only region, titania-only region, and some overlapping regions in agreement with electron micrographs.
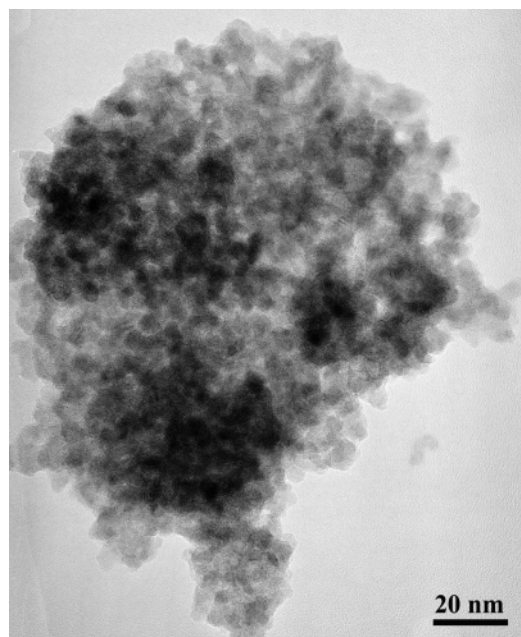
The TEM images of the CeO_2–ZrO_2 sample calcined at 773 and 1073 K are shown in Figures 11 and 12, respectively. Analyses of these and other micrographs (not shown) revealed that the grain size increased from 5 to ~10 nm with increasing calcination temperature from 773 to 1073 K. The HREM image of the sample calcined at 773 K and the corresponding DDP are shown in Figure 13. A similar HREM image was observed for the 1073 K calcined sample. The DDPs reveal crystals with well-defined bidimensional internal structures. The interplanar spacings of 3.0, 2.6, and 3.0 Å measured for the spots labeled 1, 2, and 3 (Figure 13) could be respectively assigned to (111), (200), and (1-1-1) family planes of the cubic structure. As per previous literature reports,[59,60] the fluorite cubic structure normally exhibits only three electron diffraction rings, which correspond to the interplanar spacings of ca. 3.1 (111), 2.7 (200), and 1.9 (220) Å. The other two likely phases, tetragonal and monoclinic, exhibit electron diffraction rings at or very close to these cubic spacings, as well as additional spacings. The additional spacings for the tetragonal phase are at 2.1 Å and possibly at 2.3, 3.7, and 5.3 Å (the last three being possibly active kinetic extinctions), and those for the monoclinic phase
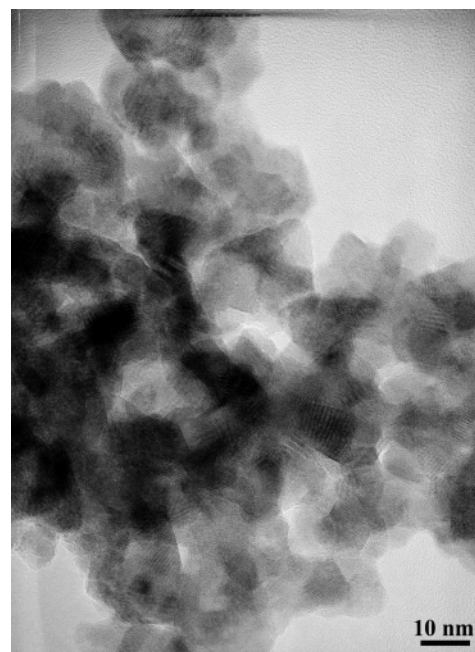
Nanosized CeO$_2$−SiO$_2$, −TiO$_2$, and −ZrO$_2$ Catalysts

J. Phys. Chem. B, Vol. 109, No. 8, 2005 **3361**

Figure 10. HREM image of CeO$_2$−TiO$_2$ sample calcined at 1073 K. The digital diffraction pattern (DDP) obtained corresponds to the TiO$_2$-only region.

Figure 11. TEM picture of CeO$_2$−ZrO$_2$ sample calcined at 773 K.

Figure 12. TEM picture of CeO$_2$−ZrO$_2$ sample calcined at 773 K.

are at 2.0−2.3, 3.7, and 5.1 Å. These spacings should be treated as approximate since they will vary slightly with the Zr content of the sample. For example, the spots at 5.3 and 5.1 Å would be difficult to separate unambiguously. The absence of any of these additional spacings clearly indicates that the Ce−Zr oxide system exists in cubic modification. Taking into account the slight contraction of the crystal lattice expected by partial substitution of Ce^{4+} ions by smaller Zr^{4+} ions, the simple fluorite type DDPs are quite obvious.[13,21,59] A significant number of crystals in the present study (Figures 11 and 12) displayed a pattern of parallel high contrast light and dark bands extending across their surfaces. As per the literature, it may be a diffraction phenomenon caused by the presence of a surface layer of different phase or different crystallographic orientation from that of the supporting crystal.[59,60] On the whole, the CeO$_2$−ZrO$_2$ sample exhibits patterns of cubic-only structures.

The potential OSCs of mixed oxides and pure CeO$_2$ (prepared by a similar soft chemical route) were evaluated by thermogravimetry. The percentage weight loss (%) and the corresponding oxygen vacancy concentration or storage capacity (δ) pertaining to various samples are presented in Table 2. As can be noted from this table, the OSCs of mixed oxide samples are

higher than the OSC of pure ceria. The high OSC of CeO$_2$−SiO$_2$ compared to CeO$_2$ could be due to the stabilization of small nanocrystals of ceria over the surface of amorphous silica matrix as observed from HREM results. As per literature reports, nanocrystalline ceria has a lower energy of reduction compared to bulk ceria and is responsible for a higher defect population.[1] Raman results strongly support this observation. Trovarelli et al. reported an improvement in the OSC of ceria due to the incorporation of small amounts of silica in the mixed ceria−silica composites.[20] In addition, it was proposed that SiO$_2$ also helps in keeping the ceria crystallites small enough to guarantee an elevated oxygen exchange. The CeO$_2$−TiO$_2$ system exhibits a slight improvement in the OSC over pure CeO$_2$. The Raman band observed at 570 cm^{-1} signifies the presence of oxygen vacancy defects in this sample. The presence of oxygen vacancies/Ce^{3+} ions in high proportions could be responsible for the high OSC observed in this mixed oxide. A predominant
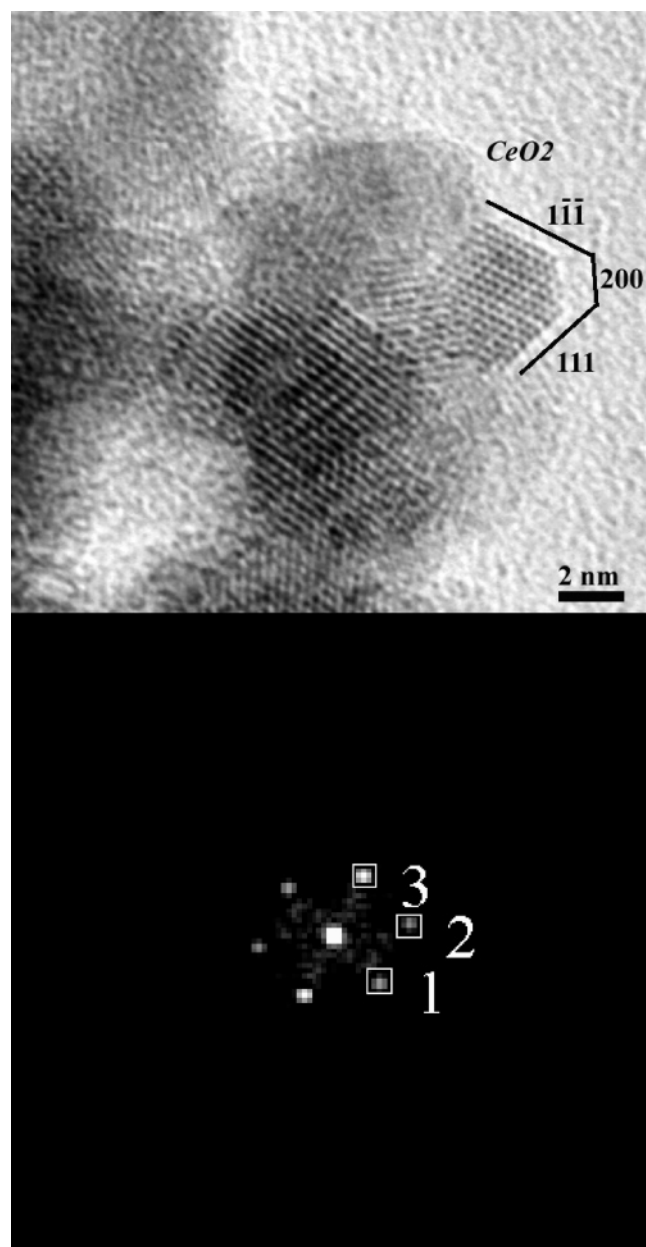
Figure 13. HREM image of CeO_2-ZrO_2 sample calcined at 773 K and digital diffraction pattern of the corresponding particles.

TABLE 2: Percentage Weight Loss and Corresponding Oxygen Vacancy Concentration, δ, in Various Samples as Determined by Thermogravimetry

sample[a]	wt loss (%)	δ
CeO_2	0.13	0.04
CeO_2-SiO_2	0.39	0.12
CeO_2-TiO_2	0.26	0.08
CeO_2-ZrO_2	0.52	0.16

[a] Calcined at 773 K.

increase in the OSC of CeO_2-ZrO_2 when compared to CeO_2 and other systems could be noted from Table 2. Distortion of O^{2-} sublattice in the mixed oxide permits a higher mobility of the lattice oxygen, and reduction is no longer confined to the surface but extends deep into the bulk.[1] From a structural point of view, there is a quite significant misfit between the ionic radii of Ce^{4+} (0.97 Å) and Zr^{4+} (0.84 Å), which is responsible for modifications of the CeO_2 lattice upon insertion of ZrO_2.[8,21] Further, the excess presence of ZrO_2 in the CeO_2 lattice at higher calcination temperatures makes the lattice more defective, which

eventually enhances the mobility of oxygen in the bulk of the CeO_2-ZrO_2 mixed oxides. The intense Raman band observed at 600 cm^{-1} supports the OSC results. On the whole, all mixed oxides exhibit better OSC properties for their eventual catalytic applications. Thus the combined XRD, Raman, HREM, and thermogravimetric studies provide valuable information on the physicochemical properties of nanosized CeO_2-SiO_2, CeO_2-TiO_2, and CeO_2-ZrO_2 mixed oxides.

Conclusions

(1) By adopting soft chemical methodologies, preparation of 1:1 mole ratio CeO_2-SiO_2, CeO_2-TiO_2, and CeO_2-ZrO_2 mixed oxide catalysts were undertaken. To evaluate the temperature stability, these oxides were subjected to thermal treatments from 773 to 1073 K and were examined by XRD, Raman, and HREM techniques. The effect of support oxides on the crystal structure of ceria was mainly contemplated.

(2) The XRD and HREM results revealed the presence of CeO_2 nanocrystals over the amorphous SiO_2 matrix in the case of CeO_2-SiO_2, whereas the CeO_2-TiO_2 sample comprised of relatively larger nanocrystals of CeO_2, TiO_2 (anatase), and some overlapped regions. The formation of cubic $Ce_{0.75}Zr_{0.25}O_2$ and $Ce_{0.6}Zr_{0.4}O_2$ phases was noted in the case of CeO_2-ZrO_2 sample.

(3) Raman measurements established the fluorite structure of ceria and the presence of oxygen vacancies/Ce^{3+}.

(4) The precise structural features of ceria nanocrystals as determined by digital diffraction analysis of the HREM experimental images revealed that the CeO_2 is mainly in the cubic fluorite geometry.

(5) The OSC studies revealed that these mixed oxides exhibit better redox properties than pure CeO_2; the redox properties depend on the nature of the mixed oxide system.

References and Notes

(1) Trovarelli, A. *Catalysis by Ceria and Related Materials*; Catalytic Science Series 2; World Scientific Publishing Company: London, UK, 2002.
(2) Bernal, S.; Kasper, J.; Trovarelli, A. Recent Progress in Catalysis by Ceria and Related Compounds. *Catal. Today* **1999**, *50*, 173.
(3) Trovarelli, A. *Catal. Rev.—Sci. Eng.* **1996**, *38*, 439 and references therein.
(4) Sato, T.; Dosaka, K.; Ishitsuka, M.; Haga, E. M.; Okuwaki, A. *J. Alloys Compd.* **1993**, *193*, 274.
(5) Sahibzada, M.; Steele, B. C. H.; Zheng, K.; Rudkin, R. A.; Metcalfe, I. S. *Catal. Today* **1997**, *38*, 459.
(6) Rossignol, S.; Madier, Y.; Duprez, D. *Catal. Today* **1999**, *50*, 261.
(7) Fornasiero, P.; Balducci, G.; Di Monte, R.; Kaspar, J.; Sergo, V.; Gubitosa, G.; Ferrero, A.; Graziani, M. *J. Catal.* **1995**, *164*, 173.
(8) Trovarelli, A.; de Leitenburg, C.; Dolcetti, G. *Chem. Tech.* **1997**, *27*, 32.
(9) Taylor, K. C. *Catalysis Science and Technology*; Springer-Verlag: Berlin, 1984; Chapter 2.
(10) Schmieg, S. J.; Belton, D. N. *Appl. Catal. B: Environ.* **1995**, *6*, 127.
(11) Di Monte, R.; Fornasiero, P.; Kaspar, J.; Graziani, M.; Gatica, J. M.; Bernal, S. Herrero, A. G. *Chem. Commun.* **2000**, 2167.
(12) Yashima, M.; Arashi, H.; Kakihana, M.; Yoshimura, M. *J. Am. Ceram. Soc.* **1994**, *77*, 1067.
(13) Reddy, B. M.; Khan, A.; Yamada, Y.; Kobayashi, T.; Loridant, S.; Volta, J. C. *Langmuir* **2003**, *19*, 3025.
(14) Rynkowski, J.; Farbotko, J.; Touroude, R.; Hilaire, L. *Appl. Catal. A: Gen.* **2000**, *203*, 335.
(15) Guglielminotti, E.; Boccuzzi, F. *J. Mol. Catal. A: Chem.* **1996**, *104*, 273.
(16) Reddy, B. M.; Khan, A.; Yamada, Y.; Kobayashi, T.; Loridant, S.; Volta, J. C. *J. Phys. Chem. B* **2003**, *107*, 5162.
(17) Bensalem, A.; Bozon-Verduraz, F.; Delamar, M.; Bugli, G. *Appl. Catal. A: Gen.* **1995**, *121*, 81.

Nanosized CeO$_2$−SiO$_2$, −TiO$_2$, and −ZrO$_2$ Catalysts

J. Phys. Chem. B, Vol. 109, No. 8, 2005 **3363**

(18) Liu, W.; Flytzani-Stephanopoulos, M. *J. Catal.* **1995**, *153*, 304.

(19) Reddy, B. M.; Khan, A.; Yamada, Y.; Kobayashi, T.; Loridant, S.; Volta, J. C. *J. Phys. Chem. B* **2002**, *106*, 10964.

(20) Trovarelli, A.; Boaro, M.; Rocchini, E.; de Leitenburg, C.; Dolcetti, G. *J. Alloys Compd.* **2001**, *323*, 584.

(21) Reddy, B. M.; Khan, A.; Yamada, Y.; Kobayashi, T.; Loridant, S.; Volta, J. C. *J. Phys. Chem. B* **2003**, *107*, 11475.

(22) Che, M.; Benett, C. O. *Adv. Catal.* **1989**, *36*, 55.

(23) Niemantsverdriet, J. W. In *Studies of Magnetic Properties of Fine Particles and their Relevance to Materials Science*; Dormann, J. L., Fiorani, D., Eds.; Elsevier: Amsterdam, 1992; p 351.

(24) Dai-Boyes, P. L. *Catal. Rev.−Sci. Eng.* **1992**, *34*, 1.

(25) Kofsta, P. *Nonstoichiometry, Diffusion and Electrical Conductivity of Binary Metal Oxides*; Wiley-Interscience: NewYork, 1972.

(26) Tschope, A.; Ying, J. Y. In *Nanophase Materials: Synthesis-Properties-Applications*; Hadjipanayis, G. C., Siegel, R. W., Eds.; Kluwer: London, 1994; p 781.

(27) Zhang, Y.; Andersson, A.; Muhammed, M. *Appl. Catal. B: Environ.* **1995**, *6*, 325.

(28) Kaspar, J.; Fornasiero, P. *J. Solid State Chem.* **2003**, *171*, 19.

(29) Zhang, F.; Chan, S.-W.; Spanier, J. E.; Apak, E.; Jin, Q.; Robinson, R. D.; Herman, I. P. *Appl. Phys. Lett.* **2002**, *80*, 127.

(30) Sugiura, M. *Catal. Surveys Asia* **2003**, *7*, 77.

(31) Yao, M. H.; Baird, R. J.; Kunz, F. W.; Hoost, T. E. *J. Catal.* **1997**, *166*, 67.

(32) Fernández-García, M.; Martínez-Arias, A.; Hungría, A. B.; Iglesias-Juez, A.; Conesa, J. C.; Soria, J. *Phys. Chem. Chem. Phys.* **2002**, *4*, 2473.

(33) Park, P. W.; Ledford, J. S. *Langmuir* **1996**, *12*, 1794.

(34) Damyanova, S.; Perez, C. A.; Schmal, M.; Bueno, J. M. C. *Appl. Catal. A: Gen.* **2002**, *234*, 271.

(35) Centeno, M. A.; Paulis, M.; Montes, M.; Odriozola, J. A. *Appl. Catal A: Gen.* **2002**, *234*, 65.

(36) Martinez-Arias, A.; Fernandez-Garcia, M.; Salamanca, L. N.; Valenzuela, R. X.; Conesa, J. C.; Soria, J. *J. Phys. Chem. B* **2000**, *104*, 4038.

(37) Ozawa, M.; Matuda, K.; Suzuki, S. *J. Alloys Compd.* **2000**, *303−304*, 56.

(38) Rocchini, E.; Trovarelli, A.; Llorca, J.; Graham, G. W.; Weber, W. H.; Maciejewski, M.; Baiker, A. *J. Catal.* **2000**, *194*, 461.

(39) Rocchini, E.; Vicario, M.; Llorca, J.; de Leitenburg, C.; Dolcetti, G.; Trovarelli, A. *J. Catal.* **2002**, *211*, 407.

(40) Klug, H. P.; Alexander, L. E. *X-ray Diffraction Procedures for Polycrystalline and Amorphous Materials*, 2nd ed.; John Wiley and Sons: New York, 1974.

(41) Ozawa, M.; Loong, C. K. *Catal. Today* **1999**, *50*, 329.

(42) Logan, A. D.; Shelef, M. *J. Mater. Res.* **1994**, *9*, 468.

(43) Preuss, A.; Gruehn, R. *J. Solid State Chem.* **1994**, *110*, 363.

(44) Hadjiivanov, K. I.; Klissurski, D. G. *Chem. Soc. Rev.* **1996**, *25*, 61 and references therein.

(45) Francisco, M. S. P.; Mastelaro, V. R. *Chem. Mater.* **2002**, *14*, 2514.

(46) Reddy, B. M.; Manohar, B.; Mehdi, S. *J. Solid State Chem.* **1992**, *97*, 7076.

(47) Anderson, C.; Bard, A. J. *J. Phys. Chem. B* **1997**, *101*, 2611.

(48) Reddy, B. M.; Ganesh, I.; Reddy, E. P.; Fernandez, A.; Smirniotis, P. G. *J. Phys. Chem. B* **2001**, *105*, 6227.

(49) Shyu, J. Z.; Weber, W. H.; Gandhi, H. S. *J. Phys. Chem.* **1988**, *92*, 4964.

(50) Lin, X.-M.; Li, L.-P.; Li, G.-S.; Su, W.-H. *Mater. Chem. Phys.* **2001**, *69*, 236.

(51) McBride, J. R.; Hass, K. C.; Poindexter, B. D.; Weber, W. H. *J. Appl. Phys.* **1994**, *76*, 2435.

(52) Spanier, J. E.; Robinson, R. D.; Zhang, F.; Chan, S.-W.; Herman, I. P. *Phys. Rev. B* **2001**, *64*, 245407.

(53) Weber, W. H.; Hass, K. C.; McBride, J. R. *Phys. Rev. B* **1993**, *48*, 178.

(54) Lepinski, L.; Wolcyrz, M. *J. Solid State Chem.* **1997**, *131*, 121.

(55) Lepinski, L.; Wolcyrz, M.; Marchewka, M. *J. Solid State Chem.* **2002**, *168*, 110.

(56) López-Cartes, C.; Pérez-Omil, J. A.; Pintado, J. M.; Calvino, J. J.; Kang, Z. C.; Eyring, L. *Ultramicroscopy* **1999**, *80*, 19.

(57) Bernal, S.; Calvino, J. J.; Cauqui, M. A.; Gatica, J. M.; Lopez-Cartes, C.; Perez-Omil, J. A.; Pintado, J. M. *Catal. Today* **2003**, *77*, 385.

(58) Francisco, M. S. P.; Mastelaro, V. R.; Nascente, P. A. P.; Florentino, A. O. *J. Phys. Chem. B* **2001**, *105*, 10515.

(59) Colon, G.; Pijolat, M.; Valdivieso, F.; Vidal, H.; Kaspar, J.; Finocchio, E.; Daturi, M.; Binet, C.; Lavalley, J. C.; Baker, R. T.; Bernal, S. *J. Chem. Soc., Faraday Trans.* **1998**, *94*, 3717.

(60) Colon, G.; Valdivieso, F.; Pijolat, M.; Baker, R. T.; Calvino, J. J.; Bernal, S. *Catal. Today* **1999**, *50*, 271.